ELSEVIER

Keratinocyte death by ferroptosis initiates skin inflammation after UVB exposure

Kavita Vats [a,1], Oleg Kruglov [a,1], Alicia Mizes [b], Svetlana N. Samovich [c], Andrew A. Amoscato [c], Vladimir A. Tyurin [c], Yulia Y. Tyurina [c], Valerian E. Kagan [c], Yuri L. Bunimovich [a,d,*]

[a] *Department of Dermatology, University of Pittsburgh, Pittsburgh, PA, 15213, USA*
[b] *School of Medicine, University of Pittsburgh, Pittsburgh, PA, 15213, USA*
[c] *Center for Free Radical and Antioxidant Health, Department of Environmental Health and Occupational Health, University of Pittsburgh, Pittsburgh, PA, 15213, USA*
[d] *Hillman Cancer Institute, University of Pittsburgh Medical Center, Pittsburgh, PA, 15213, USA*

ABSTRACT

The ultraviolet B radiation (UVB) causes skin inflammation, which contributes to the causality and the exacerbation of a number of cutaneous diseases. However, the mechanism of UVB-driven inflammation in the skin remains poorly understood. We show that ferroptosis, a non-apoptotic programmed cell death pathway that is promoted by an excessive phospholipid peroxidation, is activated in the epidermal keratinocytes after their exposure to UVB. The susceptibility of the keratinocytes to UVB-induced ferroptosis depends on the extent of pro-ferroptosis death signal generation and the dysregulation of the glutathione system. Inhibition of ferroptosis prevents the release of HMGB1 from the human epidermal keratinocytes, and blocks necroinflammation in the UVB-irradiated mouse skin. We show that while apoptosis and pyroptosis are also detectable in the keratinocytes after UVB exposure, ferroptosis plays a significant role in initiating UVB-induced inflammation in the skin. Our results have important implications for the prevention and the treatment of a broad range of skin diseases which are fostered by UVB-induced inflammation.

1. Introduction

Skin epidermis, composed primarily of the keratinocytes, sustains oxidative and genotoxic stress from the ultraviolet radiation (UVR), which causes sterile inflammation, sunburn, photoaging, and cancer [1–4]. UVR-induced inflammation, in particular, has been shown to promote tumorigenesis and metastasis of melanoma and other skin cancers, and also play a central role in the pathogenesis of lupus erythematosus [5–8]. While it is firmly established that the keratinocytes are the main initial source of pro-inflammatory mediators in the skin following ultraviolet light exposure, how UVR-induced keratinocyte injury leads to skin inflammation has not been fully determined [9–13].

Those keratinocytes which are unable to neutralize and repair UVR-induced damage undergo a regulated cell death (RCD), and apoptosis has been repeatedly demonstrated to be one such mechanism [2,14–16]. However, due to its anti-inflammatory and immunosuppressive effects, apoptosis of the keratinocytes could not account for the inflammation

after UVR exposure [13,17–21]. Cell death by regulated necrosis, in contrast to apoptosis, causes the release of immunogenic intracellular molecules into the interstitium and thereby triggers inflammation (necroinflammation) [22,23]. While research into the link between necroinflammation and disease is rapidly gaining momentum, the role of regulated necrosis in UVR-triggered cutaneous inflammation has not been established.

Several types of regulated necrosis have been described, including pyroptosis, necroptosis and ferroptosis [22,23]. Pyroptosis occurs as a consequence of the activation of caspases-1, -11, and others, and leads to cell death by cleaved gasdermin-mediated pore formation in the plasma membrane [22,24]. Necroptosis signaling pathway depends on the activation of the receptor-interacting protein kinase 3 (RIPK3), which phosphorylates mixed-lineage kinase domain-like protein (MLKL), leading to MLKL oligomerization [22,25]. Ferroptosis is a recently described RCD pathway triggered by cellular response to a changing redox environment [26,27]. In particular, the disturbed iron

---

homeostasis, deficiency of thiol-based redox regulation and the accumulation of lipid peroxidation products are three hallmarks of ferroptosis [28–31]. Cell death by ferroptosis is an immunogenic event which triggers necroinflammation [22,32]. While ferroptosis has been implicated in pulmonary and gastrointestinal chronic inflammatory diseases involving epithelial barriers, the relevance of ferroptosis to skin pathophysiology remains largely unexplored [33,34]. In vitro studies utilizing chemical inducers of oxidative stress revealed that keratinocytes can undergo ferroptosis if the glutathione or other cytoprotective systems are inhibited or overwhelmed [35,36]. Until now, however, whether epidermal keratinocytes undergo ferroptosis after UVR irradiation, and, as a result, contribute to cutaneous necroinflammation remained unanswered.

Utilizing primary human epidermal keratinocytes (HEK), human epidermal explants (HEE) and a mouse model, we show here that ferroptosis is an important non-apoptotic RCD mechanism triggered by UVR. Excessive accumulation of reactive oxygen species (ROS) and lipid peroxidation products, including the oxidized phosphatidylethanolamine (PE) ferroptosis-specific death signals, and an inadequate intracellular balance of glutathione predisposed irradiated HEK to ferroptosis. Furthermore, reduced levels of glutathione peroxidase 4 (GPX4) and elevated levels of acyl-CoA synthetase long chain 4 (ACSL4) correlated with HEK susceptibility to ferroptosis. Finally, while apoptosis and pyroptosis accounted for the death of a subset of irradiated HEK, ferroptosis was a critical RCD mode responsible for the acute UVR-driven cutaneous necroinflammation. Our results identify ferroptosis as an important mechanism of UVR-induced immunogenic death of epidermal keratinocytes, suggesting that ferroptosis may contribute to the pathogenesis of UVR-related skin diseases.

2. Results

2.1. UVB causes lipid peroxidation-dependent cell death of the keratinocytes

We assessed whether inhibitors of ferroptosis could prevent death of HEK in vitro after exposure to either UVA or UVB radiation. Lipid radical scavengers and 12/15-lipoxygenase inhibitors (ferrostatin-1, liproxstatin-1, baicalein), and long fatty acyl-CoA synthetase inhibitor (triacsin C) were utilized. All three classes of ferroptosis inhibitors were able to prevent UVB-induced death of a subset of HEK (Fig. 1A). Deferoxamine mesylate, an iron chelator and ferroptosis inhibitor, also
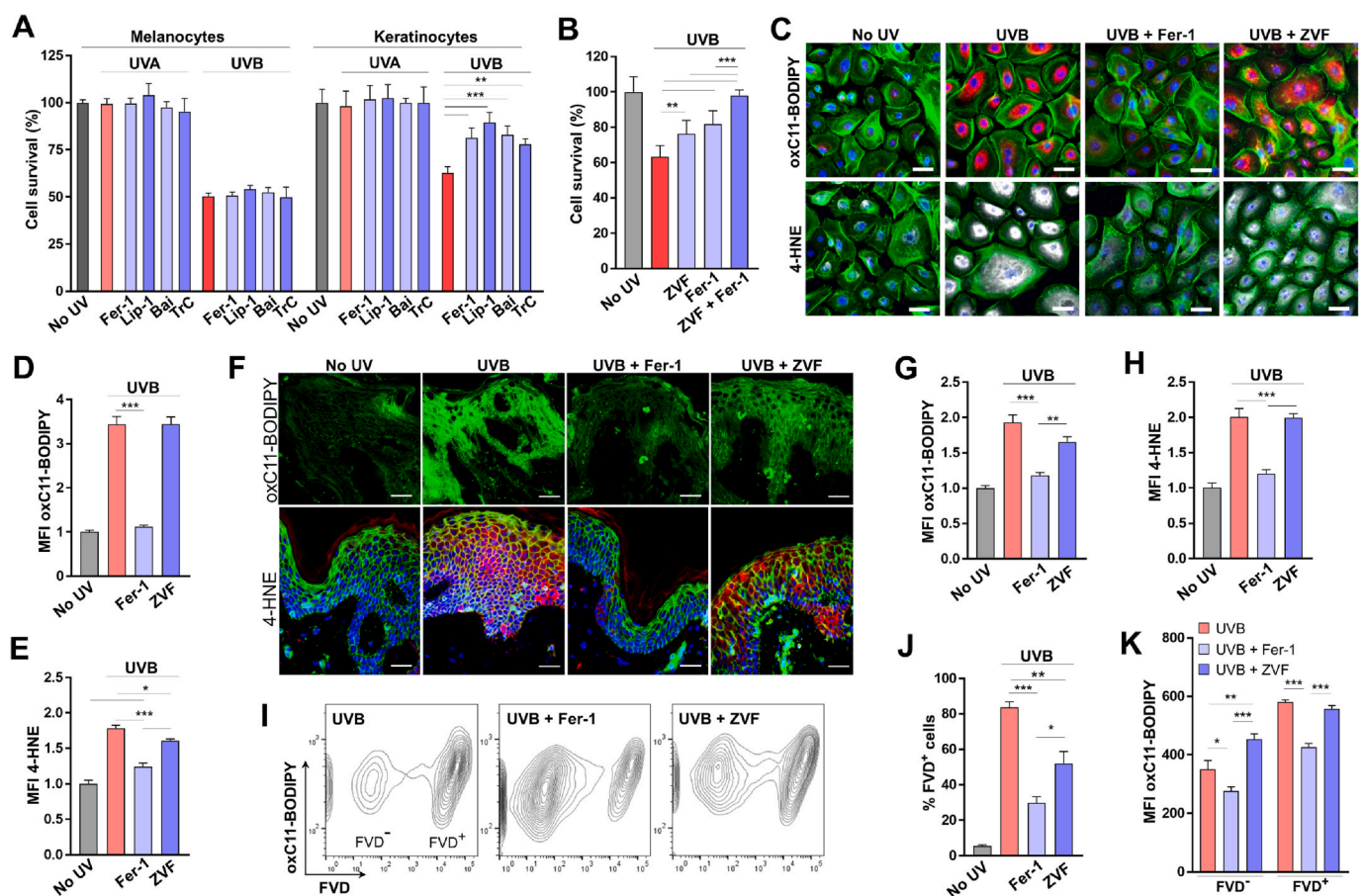
Fig. 1. UVB triggers lipid peroxidation-dependent cell death of the keratinocytes. (A) Percentage of surviving human primary melanocytes and HEK 6 h after UVA (20 kJ/m^2) or UVB (10 kJ/m^2) exposure. Cells were pretreated with ferrostatin-1 (Fer-1, 10 μM), liproxstatin-1 (Lip-1, 1 μM), baicalein (Bai, 5 μM) or triacsin C (TrC, 10 μM); n=4. (B) HEK viability 6 h after UVB exposure, pretreated with Fer-1, z-VAD-fmk (ZVF, 20 μM), or both; n=8. (C) Representative fluorescence images of HEK 6 h after UVB exposure, pretreated with either Fer-1 or ZVF, and stained for oxidized (ox)C11-BODIPY or 4-hydroxynonenal (4-HNE). Green – actin; Blue – DAPI. Scale bars: 50 μm. (D, E) Relative mean fluorescence intensity (MFI) of oxC11-BODIPY (D) or 4-HNE (E) in HEK (as in C), per 0.1 mm^2 visual field. Normalized to no UV control; n=21. (F) Representative fluorescence images of human skin explants 6 h after UVB exposure (10 kJ/m^2), pretreated with Fer-1 or ZVF and stained for either oxC11-BODIPY (top row) or 4-HNE (bottom row: red – 4HNE, green – actin). Blue – DAPI. Scale bars: 50 μm. (G, H) Relative MFI of oxC11-BODIPY (G) or 4-HNE (H) in the epidermal layer of human skin explants (as in F), per 2.0 × 10^3 μm [2] ROI; n=30. (I) Flow cytometry contour plots of HEK after UVB (10 kJ/m^2), with either Fer-1 or ZVF pretreatment, stained for oxC11-BODIPY and fixable viability dye (FVD). (J) HEK viability (measured by flow cytometry as in I); n=3. (K) MFI of oxC11-BODIPY in viable and non-viable HEK after UVB (measured as in I); n=3. Data are means ± SEM, one-way ANOVA with Tukey's multiple comparisons test. *P<0.05, **P<0.01, ***P<0.001. (For interpretation of the references to colour in this figure legend, the reader is referred to the Web version of this article.)

rescued a subset of irradiated HEK in a dose-dependent manner (Supplementary Fig. S1). Ferrostatin-1 (Fer-1) was efficacious at preventing HEK death after UVB exposure in a time- and UVB fluence-dependent manner. Specifically, Fer-1 was significantly more effective at rescuing those HEK which died relatively soon after irradiation - 6 h versus 48 h (Supplementary Fig. S2). Twenty-four hours after UVB, Fer-1 was more effective when cells were exposure to lower fluence – 2 kJ/m^2 versus 10 kJ/m^2 (Supplementary Fig. S2). In contrast to HEK, the susceptibility of the primary human melanocytes to UVB (10 kJ/m^2) was not affected by the ferroptosis inhibitors (Fig. 1A). UVA (20 kJ/m^2) did not affect the viability of HEK or the melanocytes within 6 h of the exposure. Our results suggest that a significant portion of HEK dying after UVB exposure undergo ferroptosis.

As the apoptotic death of HEK from UVB exposure has been described, we investigated whether apoptosis accounts for the death of those HEK which could not be rescued by the ferroptosis inhibitors after irradiation. Pan-caspase inhibitor z-VAD-fmk (ZVF) also rescued a significant percentage of HEK from UVB-induced death under our experimental conditions (Fig. 1B). Combining Fer-1 with ZVF prevented the death of all the UVB-irradiated HEK, measured at 6 h after the exposure (Fig. 1B). Unlike Fer-1, ZVF was more effective at 24–48 h after irradiation, irrespective of the UVB fluence (Supplementary Fig. S2).

To probe lipid peroxidation in HEK we measured intracellular oxidized C11-BODIPY and 4-hydroxynonenal (4-HNE). Oxidation of polyunsaturated butadienyl portion of C11-BODIPY by lipid pro-oxidant intermediates in cellular membrane structures to oxC11-BODIPY shifts its fluorescence emission peak [37]. A reactive lipid intermediate, 4-HNE is generated from the fragmentation of polyunsaturated fatty acid (PUFA) radicals [38]. HEK exposure to UVB led to the oxidation of C11-BODIPY and the generation of 4-HNE, which were inhibited by Fer-1 but not by ZVF (Fig. 1C–E). In addition, UVB-induced increases in 4-HNE and oxC11-BODIPY within the epidermal layer of the human skin explants were prevented by Fer-1 treatment, but not ZVF, prior to irradiation (Fig. 1F–H). We utilized flow cytometry to measure intracellular accumulation of fixable viability dye (FVD) to identify non-viable cells with damaged cell membranes, and a concomitant oxidation of C11-BODIPY (Fig. 1I). Both Fer-1 and ZVF significantly reduced FVD accumulation in HEK after UVB, but only Fer-1 reduced oxC11-BODIPY (Fig. 1I–K). Taken together, our results indicate that after UVB exposure the majority of the dying HEK undergo either caspase- or lipid peroxidation-dependent RCD, particularly implicating apoptosis, pyroptosis and ferroptosis mechanisms.

2.2. UVB causes the accumulation of ferroptosis-specific oxygenated phospholipids in the keratinocytes

Excessive accumulation of lipid peroxides is the hallmark of cellular demise by ferroptosis. Specifically, hydroperoxy-derivatives of arachidonoyl- or adrenoyl-phosphatidylethanolamines (AA-PE, AdA-PE, respectively) are highly specific signals of ferroptosis [31]. To reveal the changes in the lipidome of HEK after UVB, we performed global redox phospholipidomics analysis. We detected 306 phospholipid (PL) molecular species, including 93 oxygenated PL species. To quantitatively evaluate the effects of UVB and UVB in the presence of Fer-1 (UVB + Fer-1) on PL oxidation, we used multivariate analysis. First, all identified lipids were subjected to principal component analysis (PCA) to assess the differences in the lipidome between the groups. PCA revealed that control (No UV) HEK and HEK + UVB + Fer-1 clustered tightly, while HEK + UVB without Fer-1 showed some heterogeneity in the lipids (Supplementary Fig. S3A). Next, we used orthogonal projection of latent structures - discriminant analysis (OPLS-DA) to reveal the driving forces among the variables detected in lipidome. The score plots in OPLS-DA showed good clustering of control HEK and HEK + UVB, as well as HEK + UVB and HEK + UVB + Fer-1 (Supplementary Fig. S3B1, C1). We used S-plots to show variable correlation versus variable contribution of the OPLS-DA model (Supplementary Fig. S3B2, C2) and

variable importance in projection (VIP) score plots to reflect the significance of OPLS-DA variables (Supplementary Fig. S3B3, C3). In line with our published data demonstrating that ferroptosis is mainly associated with high levels of oxygenated phosphatidylethanolamine (PEox), along with accumulation of peroxidized phosphatidylinositol (PIox) and phosphatidylserine (PSox) species [39], we found that PEox, PIox and PSox positively contributed to the lipidome differences between control HEK and HEK + UVB (Supplementary Fig. S3B2). PE-38:5-OOH and PI-38:2-OOH were among the top ten PL metabolites responsible for the differences between control HEK and HEK + UVB, with highest VIP scores of 1.671 and 1.670, respectively. In addition, five hydroxy-PLs: PE-36:2-OH, PE-38:3-OH, PE-38:5-OH, PI-36:2-OH and PS-40:5, with VIP scores of 1.665, 1.664, 1.660, 1.660 and 1.636, respectively, strongly contributed to lipidome differences between control HEK and HEK + UVB (Supplementary Fig. S3B).

We also found negative correlation in these oxygenated species between HEK + UVB and HEK + UVB + Fer-1 groups, implying their decrease in the presence of Fer-1 (Supplementary Fig. S3C2). It should be noted that these changes in PLs were specific as not all oxygenated PLs were related to ferroptosis. Oxygenated species of phosphatidylcholine (PC), the most abundant class of PLs, did not contribute to the differences between the three groups. The amounts of only three PCox species were slightly increased upon UVB exposure, and were not affected by Fer-1. Overall, OPLS-DA revealed that oxygenated PL species, particularly those related to ferroptosis, were major contributors to UVB-related differences in the lipidomes.

Redox lipidomics analysis revealed the presence of oxygenated species of PE-(18:1/20:4) in HEK and PE-(18:0/20:4) in HEE (Fig. 2A–D and 2E-G, respectively) in the short range of *m/z* for control (no UVB), UBV, and UBV + Fer-1 groups. The MS/MS analysis verified the structure of oxidized PLs, PE-38:5-OOH and PE-38:4-OOH (Supplementary Fig. S4). Precursors of ferroptotic death signals, oxidizable PE species with *m/z* 764.5 and 766.5 corresponding to PE-(18:1/20:4) and PE-(18:0/20:4), were readily detectable in HEK and in HEE (Fig. 2A, E; Supplementary Fig. S4). No significant changes in the content of these precursors after UVB exposure were found. Amounts of PL species were normalized to total PLs and presented as pmol/nmol of total PLs for oxidizable species and as pmol/μmol of total PLs for oxygenated PLs. Levels of PE-(18:1/20:4) in HEK were 1.30 ± 0.06 and 1.21 ± 0.04 pmol/nmol of total PLs before and after UVB, respectively. Levels of PE-(18:0/20:4) in HEE before and after UVB were 3.72 ± 0.09 and 3.70 ± 0.5 pmol/nmol of total PLs, respectively. Total PEox species in control HEK and HEE comprised 1720.1 ± 62.0 pmol/μmol of total PLs and 587.4 ± 249.8 pmol/μmol of total PLs, respectively. Thus, total PEox were 0.17 ± 0.01% and 0.06 ± 0.03% of total PLs in control HEK and HEE, respectively. After UVB exposure, total PEox were increased to 0.22 ± 0.01% (HEK) and 0.09 ± 0.01% (HEE) of total PLs, respectively.

Oxygenated PE species in HEK (Fig. 2A–C, Supplementary Fig. S5) comprised four of the top ten PL metabolites responsible for lipidome differences between the groups (Supplementary Figs. S3B and C). Among PEox, hydroperoxy-PE species (PE-38:5-OOH), which were previously identified as ferroptotic cell death signals, were significantly elevated after UVB (Fig. 2D), and demonstrated the highest VIP scores for positive and negative correlations (Supplementary Fig. S3 B3, C3). Similar changes in PEox levels, and particularly in the ferroptosis-specific (PE-38:4-OOH) species, were observed in HEE upon UVB exposure (Fig. 2E–H, Supplementary Fig. S6). Thus, PEox species characteristic of ferroptosis were major contributors to the differences between control and UVB groups as well as between UVB and UVB + Fer-1 groups.

Taking into account that UVB exposure induces apoptosis and oxygenated polyunsaturated cardiolipins (CLox) were identified as apoptotic cells death signals [40,41], we analyzed CL molecular species in HEK and HEE (Fig. 3). In HEK, CLs were mainly represented by non-oxidizable species containing mono-unsaturated fatty acids such as palmitoleic (C16:1) and oleic (C18:1) (Fig. 3A). Thus, we were not able
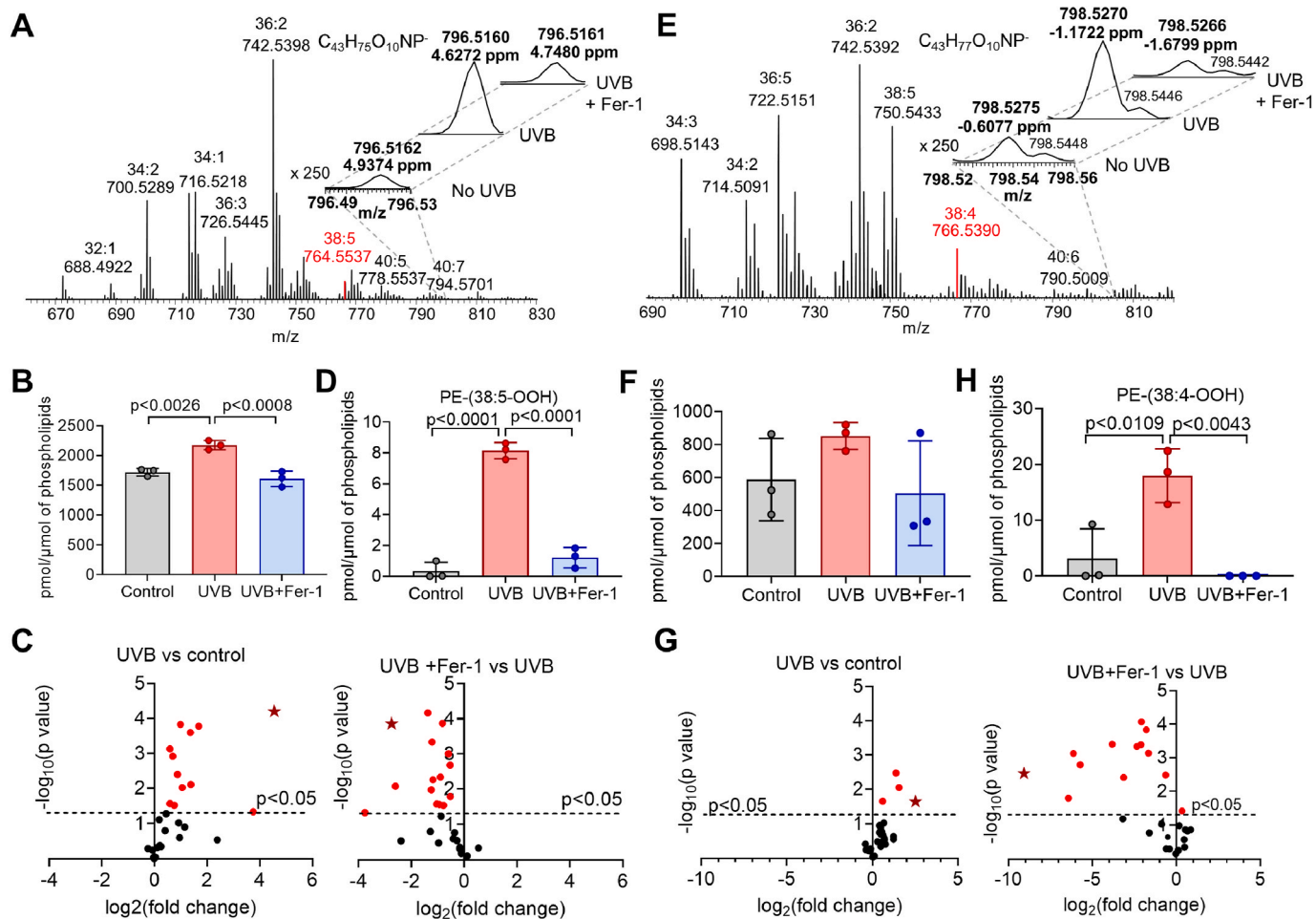
Fig. 2. UVB induces ferroptotic cell death signals in HEK and HEE. (A) Typical mass spectra of phosphatidylethanolamine (PE) species obtained from HEK with LC-MS. Oxidizable PE-(18:1/20:4) species with m/z 764.5537 shown in red. MS spectra for oxygenated species PE-(18:1/20:4) in the range of m/z from 798.52 to 792.56 (insert). (B) Effect of Fer-1 (10 μM) on UVB-induced (10 kJ/m^2) accumulation of total oxygenated PE (PEox) species in HEK 6 h after irradiation. (C) Volcano plots of UVB-induced changes in the levels of PEox molecular species in HEK. Stars designate ferroptotic death signal - PE-(38:5-OOH) (quantified in D). (D) Effect of Fer-1 on UVB-induced accumulation of PE-(38:5-OOH) in HEK. (E) Typical mass spectra of PE species obtained from HEE with LC-MS. Oxidizable PE-(18:0/20:4) species with m/z 766.5390 shown in red. MS spectra for oxygenated species PE-(18:0/20:4) in the short range of m/z from 796.49 to 796.53 (insert). (F) Effect of Fer-1 on UVB-induced accumulation of PEox species in HEE. (G) Volcano plots of UVB-induced changes in PEox levels in HEE. Stars designate ferroptotic death signal - PE-(38:4-OOH) (quantified in H). (H) Effect of Fer-1 on UVB-induced accumulation of PE-(38:4-OOH) in HEE. Mass spectra of PE obtained from HEK and HEE contain ten and seven clusters of signals, respectively. The upper numbers in the MS spectra of PE indicate the summed number of carbon atoms at *sn-1* and *sn-2* positions and the summed number of double bonds in both fatty acids. The lower numbers correspond to m/z values which indicate ratios of mass to charge for singly charged [M − H]⁻ ions. (For interpretation of the references to colour in this figure legend, the reader is referred to the Web version of this article.)

to detect CLox species in HEK. In contrast, in HEE CL species were enriched in highly oxidizable linoleic (C18:2) acid (Fig. 3B). Fifty-four CLox molecular species were detected in control HEE (Supplementary Fig. S7), comprising 87.5 ± 11.0 pmol/μmol (0.009 ± 0.001%) of total PLs. UVB exposure increased total CLox in HEE to 127.5 ± 5.5 pmol/μmol (0.013 ± 0.001%) of total PLs. We found that in HEE exposed to UVB the contents of CLox were higher compare to control HEE (Fig. 3C; Supplementary Fig. S7). Analysis of individual CL species revealed the accumulation of CLox species that were previously identified as apoptotic signals (Fig. 3D). Interestingly, treatment with Fer-1, a scavenger of lipid radicals, protected against UVB-induced accumulation of CLox species (Fig. 3C and D; Supplementary Fig. S7). Taken together, these results confirm that UVB induces changes in the content of PEox and CLox species in HEK and HEE which are required for the execution of ferroptosis and apoptosis, respectively.

2.3. UVB-induced redox dysregulation contributes to keratinocyte death by ferroptosis

We investigated how UVB exposure may predispose HEK toward ferroptosis. As expected, UVB induced robust generation and release of ROS by HEK, which was significantly diminished by the ferroptosis inhibitors (Fig. 4A). In both HEK and HEE, UVB led to a significant decrease in the intracellular levels of the reduced form of glutathione (GSH), consistent with previous reports (Fig. 4B and C) [42]. Ferroptosis inhibitors, but not ZVF, prevented the depletion of GSH (Fig. 4B and C). Therefore, dysregulated glutathione system, either due to an accelerated GSH consumption or an insufficient synthesis, accounts for HEK susceptibility to UVB-induced ferroptosis.

We next examined how UVB exposure affects known regulators of ferroptosis. Specifically, we concentrated on ACSL4 and 15-lipoxygenase (15-LOX) as these are critical to AA-PE synthesis and enzymatic oxidation, respectively. In addition, we examined cystine-glutamate antiporter, system x_C^-, and glutathione peroxidase 4 (GPX4) because of their roles in the maintenance and utilization of GSH for lipid
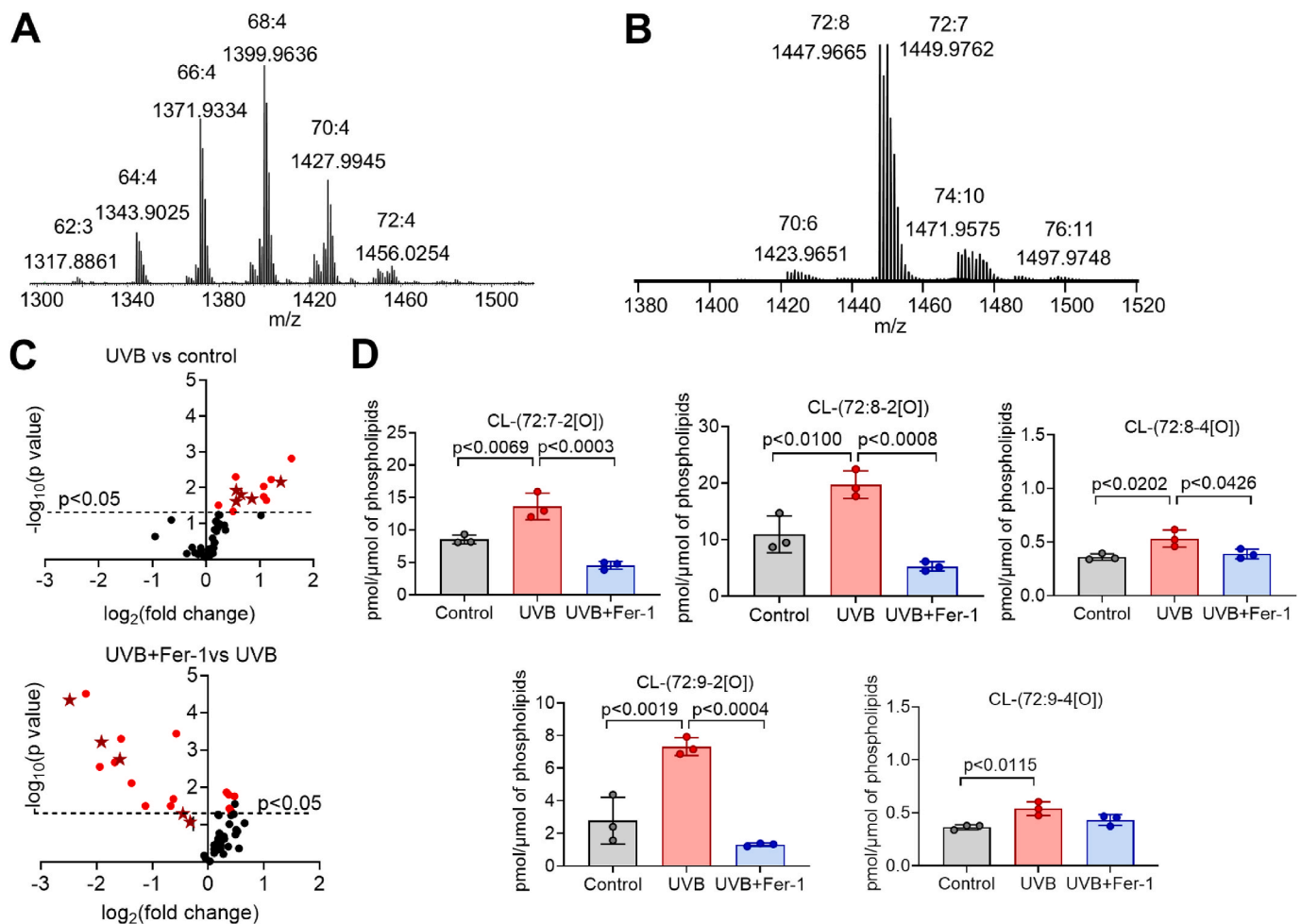
Fig. 3. UVB leads to cardiolipin oxidation in HEK and HEE. (A, B) Typical mass spectra of cardiolipin (CL) obtained from HEK (A) and HEE (B). Mass spectra of CL obtained from HEK and HEE contain six and four clusters, respectively. The upper numbers in the MS spectra of CL indicate the summed number of carbon atoms and the summed number of double bonds in four fatty acid residues. The lower numbers correspond to *m/z* values which indicate ratios of mass to charge for singly charged [M − H]⁻ ions. (C) Volcano plots of UVB (10 kJ/m²) -induced changes in the level of oxygenated CL molecular species in HEE. Stars indicate apoptotic death signals CL-(72:7–2[O]); CL-(72:8–2[O]); CL-(72:8–4[O]); CL-(72:9–2[O]); CL-(72:9–4[O]) (quantified in D). (D) Effect of Fer-1 (10 μM) on UVB induced accumulation of oxygenated CL species in HEE.

hydroperoxide radical reduction. Expression of ACSL4, 15-LOX and GPX4 by HEK increased after UVB exposure, while SLC7A11 (xCT, the light chain subunit of system x$_C^-$) was unaffected (Fig. 4D). Fer-1 reduced (GPX4) or completely prevented (ACSL4, 15-LOX) UVB-induced upregulation of the expression of these genes in HEK (Fig. 4D). However, on a protein level xCT and 15-LOX were unaffected by UVB 6 h after irradiation, while GPX4 decreased and ACSL4 increased (Fig. 4E and F). Supplementing cell media with cystine rescued a modest percentage of cells in a dose-dependent manner, suggesting that limited cystine transport is partially responsible for intracellular GSH depletion after UVB (Supplementary Fig. S8). We also considered that DNA damage response (DDR) initiated by UVB may modulate ferroptosis in HEK. Indeed, p53 activation triggered by DDR has been shown to regulate ferroptosis via several mechanisms, including the downregulation of SLC7A11 [43]. While we did not observe changes in SLC7A11 expression, we examined two markers of DDR, phosphorylated γ-H2A.X and p53, in HEK after UVB exposure. We detected a clear UVB-induced DDR in HEK, which was not affected by either Fer-1 or ZVF (Supplementary Fig. S9).

We further utilized flow cytometry to examine GPX4 and ACSL4 in HEK after UVB exposure, which allowed us to correlate protein levels with the integrity of the cellular membrane (viability) of individual cells (Fig. 4G). Specifically, intracellular accumulation of FVD was used to

identify non-viable cells with damaged cell membranes. We confirmed that UVB exposure increases 4-HNE in HEK, and that non-viable FVD⁺ HEK had significantly higher accumulation of lipid peroxidation products compared to viable FVD⁻ HEK (Fig. 4H). Furthermore, irradiated FVD⁺ cells contained more ACSL4 and less GPX4 compared to irradiated viable cells and control (Fig. 4H). Fer-1 treatment of HEK before UVB exposure, but not ZVF, decreased 4-HNE in FVD⁺ cells, indicating that a subset of cells which were rescued by Fer-1 contained high amounts of lipid peroxidation products (Fig. 4I). The same subset of HEK which were rescued by Fer-1, but not ZVF, contained relatively less GPX4 and more ACSL4 (Fig. 4I). Finally, in irradiated HEE we noticed a strong correlation between ACSL4 levels and 4-HNE, but not between GPX4 and 4-HNE (Fig. 4J and K). Taken together, our results suggest that keratinocyte susceptibility to ferroptosis after UVB exposure is dictated by the degree of lipid peroxidation and the availability of glutathione.

2.4. Lipid peroxidation is a critical driver of an immunogenic UVB-induced keratinocyte death

While an excessive lipid peroxidation is critical for the execution of ferroptosis, some degree of lipid peroxidation has also been described in apoptosis, necroptosis and pyroptosis [39,40,44,45]. We investigated whether these modes of RCD occur in HEK within 6 h of UVB exposure.
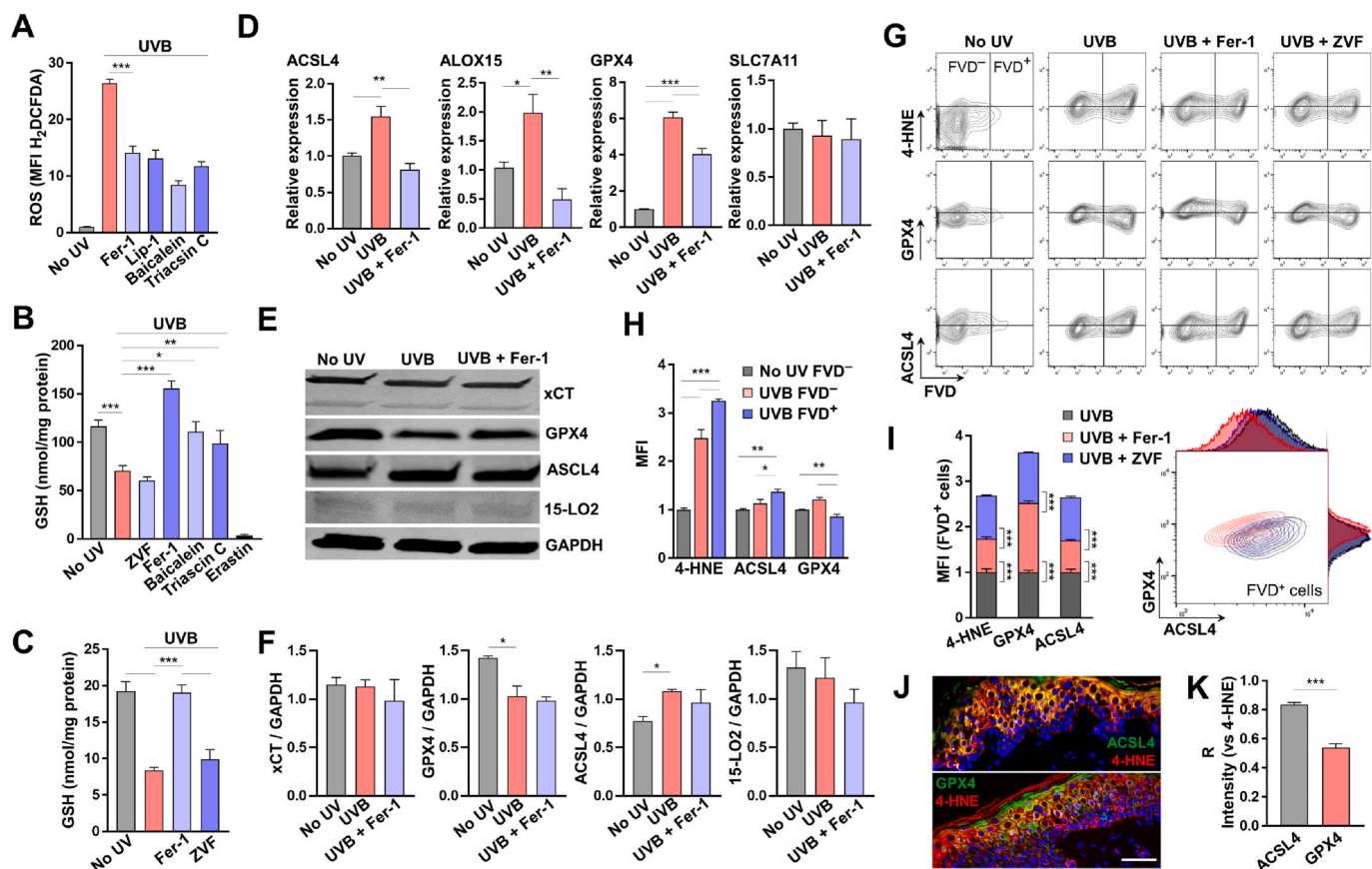
Fig. 4. UVB-induced redox dysregulation leads to ferroptosis of the keratinocytes. (A) Intracellular ROS in HEK, measured using 2',7'-dichlorodihydro-fluorescein diacetate - H2DCFDA, 6 h after UVB (10 kJ/m^2) relative to control (no UV), with Fer-1 (10 μM), triascin C (10 μM) or baicalein (5 μM); n=6. (B, C) Glutathione (GSH) in HEK (B) or HEE (C) 6 h after UVB, with Fer-1 (10 μM), triascin C (10 μM), baicalein (5 μM), ZVF (20 μM), or erastin (10 μM); n=6. (D) Relative expression of *ACSL4*, *ALOX15*, *GPX4*, *SLC7A11* in HEK 6 h after UVB, determined by qRT-PCR; n = 6. (E) Representative Western blots of ACSL4, 15-LOX, GPX4, xCT in HEK 6 h after UVB. GAPDH used as control. (F) Densitometry of the Western blots shown in (E), normalized to GAPDH; n=2. (G) Representative flow cytometry contour plots of HEK after UVB labeled with FVD and co-stained for 4-HNE, GPX4, and ACSL4. (H) MFI of contour plots shown in (G), UVB-exposed vs. no UV control HEK; n=3. (I) MFI (left) or contour/histogram plot (right) of non-viable UVB-exposed HEK (as in G); n=3. (J) Representative fluorescence images of human skin explants 6 h after UVB (10 kJ/m^2). Red – 4HNE, Green – ACSL4 or GPX4, Blue – DAPI. Scale bars: 50 μm. (K) Correlation coefficient of a linear intensity profile of the epidermis obtained from (J), ACSL4 or GPX4 vs. 4-HNE; n=6. Data are means ± SEM; one-way ANOVA with Tukey's multiple comparisons test. *P<0.05, **P<0.01, ***P<0.001. (For interpretation of the references to colour in this figure legend, the reader is referred to the Web version of this article.)

We detected neither the autophosphorylated form of RIPK-3 nor its phosphorylation target MLKL after irradiation, suggesting that necroptosis is not involved in UVB-triggered HEK death (Fig. 5A). Caspases 1 and 3 were activated after UVB exposure, and Fer-1 pretreatment prevented the cleavage of caspase-1 but not caspase-3, while pan-caspase inhibitor ZVF blocked the activation of both caspases (Fig. 5B). Inflammasome-activated caspase-1 cleaves pro-IL-1β to IL-1β and gasdermin D (GSDMD), releasing GSDMD N-terminal domain which forms pores in plasma membrane and induces pyroptotic cell death [24]. We detected caspase-1 activation and IL-1β cleavage in HEK after UVB, but we could not detect cleaved GSDMD either in HEK (Fig. 5B) or in HEE, consistent with published report [46]. The cleavage of gasdermin E, a substrate of caspase-3, was detected after UVB and, as with caspase-3 activation, could be blocked by ZVF but not by Fer-1 (Fig. 5B).

Flow cytometry was utilized to further delineate the effects of Fer-1 and ZVF on caspase activation in UVB-exposed HEK. Consistent with Western blot analysis, both Fer-1 and ZVF decreased the percentages of irradiated FVD$^+$ cells with activated caspase-1 (Fig. 5C and D). Fer-1 was, however, significantly more effective compared to ZVF at rescuing FVD$^+$ cells without cleaved caspase-1 (Fig. 5C and D). Flow cytometry for activated caspase 3 was also consistent with our Western blot data. Specifically, Fer-1, in contrast to ZVF, did not rescue FVD$^+$ cells with activated caspase 3, but was, again, significantly more

effective at rescuing irradiated HEK without activated caspase 3 (Fig. 5E and F). Taken together, our results suggest that UVB induces ferroptosis, apoptosis and pyroptosis, but not necroptosis, in HEK, and confirm published data that Fer-1, unlike ZVF, has no effect on the execution of apoptosis and pyroptosis [39].

Next, we examined the release of high mobility group box protein (HMGB)-1 from HEK after irradiation with UVB. HMGB-1 is a proto-typical damage-associate molecular pattern (DAMP) signal and a common marker of necroinflammation. UVB triggered a robust release of HMGB1 from HEK and HEE, which could be blocked by Fer-1 but not by ZVF (Fig. 5G and H). Considering orthogonal effects of Fer-1 and ZVF on ferroptosis, apoptosis and pyroptosis, our results suggest that the release of danger signals from UVB-exposed keratinocytes is driven, to a large extent, by ferroptotic cell death.

2.5. Keratinocyte death by ferroptosis after UVB exposure induces skin necroinflammation

Having established that ferroptosis execution in HEK after UVB exposure releases HMGB1 danger signal, we investigated whether fer-roptotic death of HEK causes necroinflammation after skin irradiation. Topical pre-treatment of C57BL/6 mice with Fer-1, but not with ZVF, significantly decreased 4-HNE within the epidermal layer after UVB
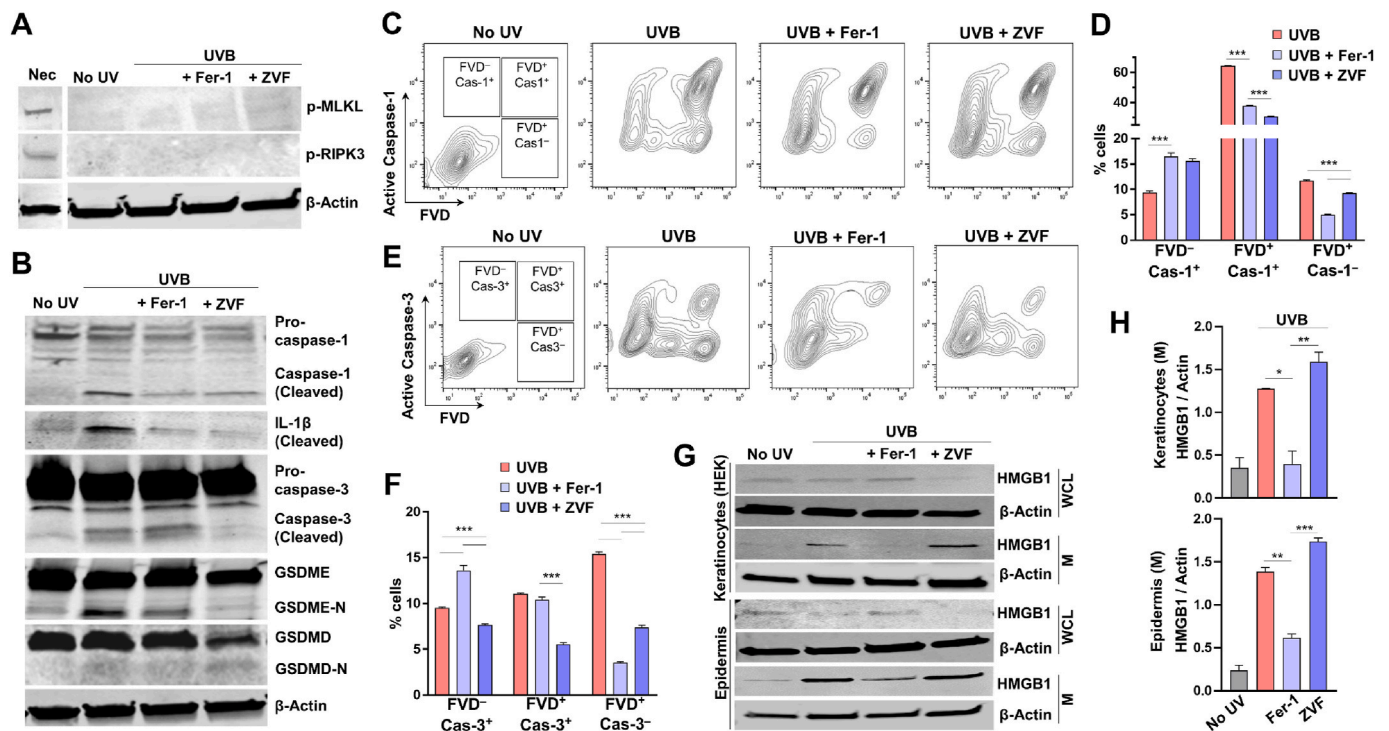
Fig. 5. Immunogenic keratinocyte death after UVB exposure is due to ferroptosis. (A) Western blots of HEK for necroptosis markers after UVB (10 kJ/m^2). Left column (Nec): necroptosis was induced in HEK with 4000IU/ml hTNF, 5 µM TPCA-1 and 15 µM z-VAD-fmk for 18 h. (B) Western blots of cleaved caspases 1 and 3, and their downstream targets in HEK after UVB. (C) Flow cytometry contour plots of HEK viability after UVB vs. activated caspase-1. (D) Percentages of HEK in indicated sub-populations (as in C); n=3. (E) Flow cytometry contour plots of HEK viability after UVB vs. activated caspase-3. (F) Percentages of HEK in indicated sub-populations (as in E); n=3. (G) Western blots of HMGB1 from HEK or HEE, either measured in whole cell lysates (WCL) or culture media (M). (H) Densitometry from the Western blots shown in (G) of HMGB1 in culture media (M), normalized to actin; n=2. Data are means ± SEM; one-way ANOVA with Tukey's multiple comparisons test. *P<0.05, **P<0.01, ***P<0.001.

(Fig. 6A and B), consistent with the results from human skin explants (Fig. 1F–H). Histological examination of the irradiated mouse skin revealed a dermal immune cell infiltrate, which was significantly diminished by topical Fer-1 treatment prior to UVB, but not by ZVF (Fig. 6C and D). Flow cytometry was used to characterize skin immune infiltrate 24 h after UVB (Supplementary Fig. S10), which was primarily composed of CD11b$^+$Ly6G$^+$ neutrophils and F4/80$^+$ macrophages, with CD3$^+$ lymphocytes comprising a small percentage of the total leukocytes (Fig. 6E). The presence of these myeloid populations in the irradiated skin pretreated with Fer-1, but not with ZVF, was significantly diminished (Fig. 6E).

To further characterize Fer-1 effect on UVB-induced cutaneous necroinflammation, we measured the expression of select cytokines in the irradiated mouse skin. Interleukins 6, 1β, 10 and 18, known to be upregulated in the skin within 24 h of UVB exposure [47–49], were expressed at significantly lower levels in the irradiated skin treated with Fer-1 compared to vehicle or ZVF treated skin (Fig. 6F). Taken together, our results demonstrate that ferroptotic death of the epidermal keratinocytes is a critical driver of UVB-induced necroinflammation in the skin.

3. Discussion

Local and systemic immunomodulation by UVR may paradoxically exacerbate or ameliorate malignant, autoimmune, inflammatory and infectious skin diseases [50]. For example, UVR-induced inflammation and immunosuppression have both been implicated in the initiation and progression of skin cancer [7,51]. Autoimmune and inflammatory diseases such as lupus erythematosus and psoriasis, respectively, are clearly exacerbated by UV exposure of the skin, while UVA and UVB have been utilized as a treatment modality for the same conditions [5,52,53]. Such

opposing UV effects are based, at least in part, on how damaged keratinocytes succumb to radiation, as different cell death mechanisms initiate varying immune responses [50,54]. While apoptotic death is widely considered to be an immunosuppressive event, the release of pro-inflammatory DAMPs by the keratinocytes following exposure to UVR has been largely attributed to an unregulated necrosis [6,13,14]. We show here that ferroptosis, a type of programmed non-apoptotic cell death – a regulated necrosis, is responsible for immunogenic keratinocyte death following UVB exposure which leads to skin necroinflammation.

The narrow band (310 nm) UVB dosages utilized in our study (2–10 kJ/m^2) are consistent with typical broad band solar irradiance on the earth's surface [55]. It is also consistent with narrow band UVB dosages utilized in the clinical setting (500–1000 mJ/cm^2) [56]. Other studies examining the effects of UVB on different types of cells, including the keratinocytes, have utilized similar fluences [57–60].

Keratinocyte death by ferroptosis, to our knowledge, has never before been demonstrated in the context of UV irradiation. This is possibly in part due to the challenges in differentiating ferroptosis from other modes of RCD. Ferroptosis cytotoxicity, in contrast to other RCD pathways, depends on excessive and specific phospholipid peroxidation, which is averted with lipid alkoxyl radical scavengers such as Fer-1. To provide further evidence for ferroptosis in the keratinocytes in vitro and in vivo, we carried out analyses of lipid peroxidation using fluorescent probes and oxidative lipidomics, a gold standard method to identify particular oxidized lipid species. Ferroptosis was detected in vitro and in vivo in a subset of UVB irradiated HEK, where Fer-1 prevented death by inhibiting an excessive accumulation of lipid peroxidation products, including specifically the hydroperoxy-derivatives of AA-PE.

UVB can cause the generation of singlet oxygen, and consequently induce the accumulation of PL hydroperoxides. This explains, at least in
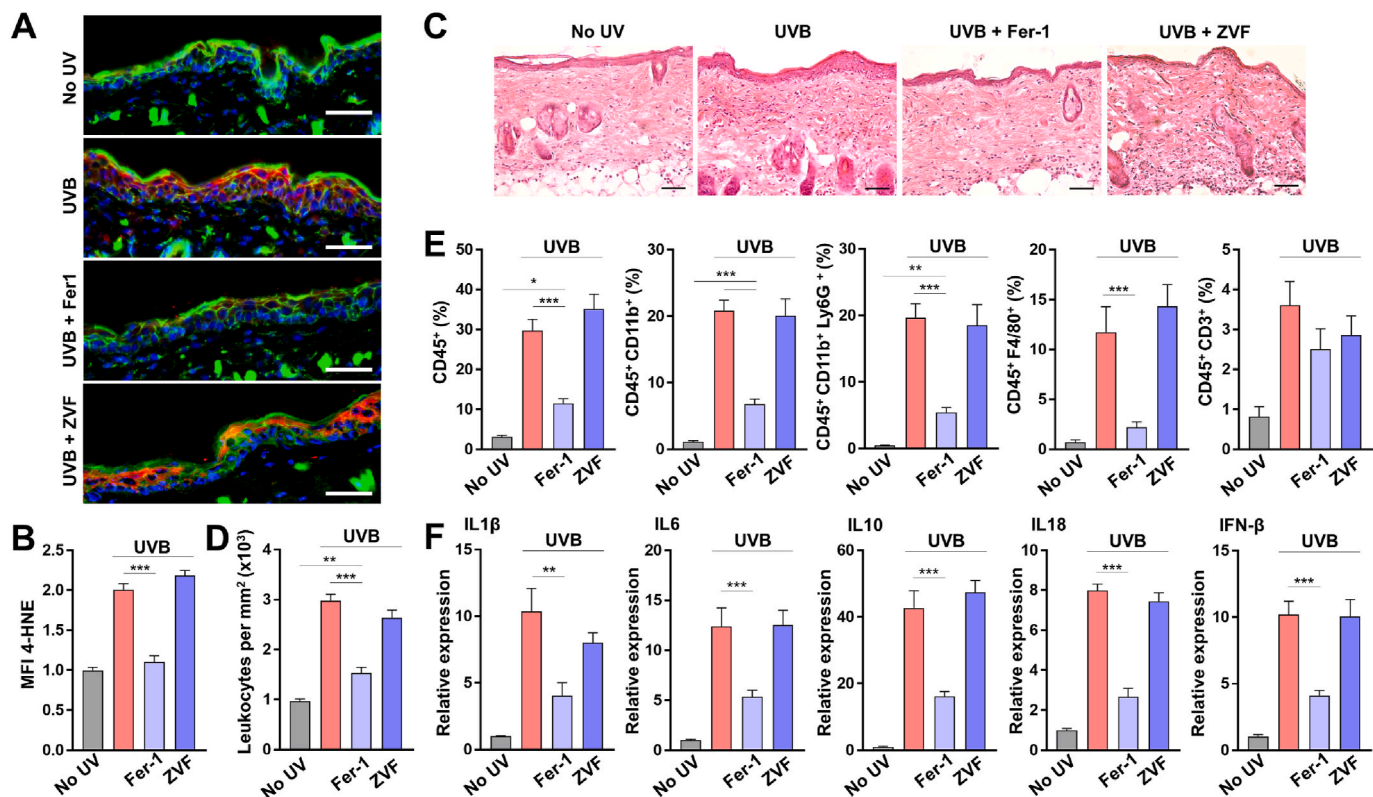
Fig. 6. Keratinocyte ferroptosis after UVB leads to skin necroinflammation. (A) Representative fluorescence images of C57Bl/6 mouse skin 6 h after UVB (5 kJ/m^2), and pre-treated with either vehicle (No UV and UVB groups), ferrostatin-1 (Fer1, 10 μM) or z-VAD-fmk (ZVF, 20 μM). Red – 4HNE, Green – Actin, Blue – DAPI. Scale bars: 50 μm. (B) Relative MFI of 4-HNE in the epidermal layer of mouse skin shown in A, per 5.0×10^2 μm [2] ROI; n=10. (C) Mouse skin (H&E) 16 h after UVB. Scale bars: 50 μm. (D) Leukocyte density in mouse skin shown in C; n=5. (E) Skin infiltration by several populations of immune cells 16 h after UVB (5 kJ/m^2), measured by flow cytometry. Percentages of total cells are shown; n=15. (F) Relative expression of cytokines in mouse skin 16 h after UVB; n=15. Data are means ± SEM; one-way ANOVA with Tukey's multiple comparisons test. *P<0.05, **P<0.01, ***P<0.001. (For interpretation of the references to colour in this figure legend, the reader is referred to the Web version of this article.)

part, higher contents of hydroperoxy-PE species, including the species containing 15-hydroperoxy-arachidonic acid (15-HpETE-PE), upon the exposure of HEK and HEE to UVB. Our previous work with GPX4-and ACSL4-deficient fibroblasts identified 15-HpETE-PE species as specific signals of ferroptosis [31]. Subsequent studies demonstrated that ferroptosis-specific PLox species may vary in different cell lines and primary cells and include PSox and PIox, although both the number and amounts of PEox species remained the most significant diagnostic feature of ferroptosis [39]. While Fer-1 is universally considered and used as a selective inhibitor of ferroprosis that effectively inhibits 15LOX/PEBP1 complex involved in 15-HpETE-PE production during the execution of ferroptosis [61–63], it also acts as a broader lipophilic radical scavenger [64]. In the current work, by using OPLS-DA analysis of oxygenated PLs from control and UV-exposed HEK we found that, in addition to hydroperoxy-PE (PE-38:5-OOH), hydroperoxy-PI (PI-38:2-OOH) and five hydroxy-PLs: PE-36:2-OH, PE-38:3-OH, PE-38:5-OH, PI-36:2-OH and PS-40:5 positively correlated with UVB-induced ferroptosis, with the highest VIP scores. Accumulations of all these species were prevented by Fer-1. Therefore, while Fer-1 is not a selective scavenger of 15-HpETE-PE-derived radicals, our results demonstrate that ferroptosis-specific PEox signals are among the top contributors to the differences between the lipidomes of the control and UVB-treated HEK.

Enzymatic dioxygenase reactions and non-enzymatic free radical peroxidation leading to the production of PL hydroperoxides proceed during normal cell and tissue metabolism. Lipid peroxidation products, including lipid hydroperoxides, have been detected in the keratinocytes at baseline, and generally found to be elevated in response to chemical and physical prooxidants [65–67]. Recent developments in high

resolution and high mass accuracy liquid chromatography-mass spectrometry (LC-MS) platforms and new software packages [68] permitted the detection and the analysis of lipid oxidation products at very low abundance (~0.1–1.0% of the respective non-oxidized PLs). In this work, we determined PEox and CLox to be below 0.2% of total PLs at baseline in control HEK and HEE, consistent with previous reports [65–67]. It should be noted that the oxygenated pro-ferroptotic and pro-apoptotic PLs may serve as specific signals interacting with their target membrane (macro)molecules by acting as ligands, or by forming covalent adducts generated from the primary hydroperoxy-lipids. In the latter case, detected amounts of these non-adducted products may represent only a fraction of all peroxidized lipids. Future work in the field of redox lipidomics will quantitatively address these important issues [69].

We show that ferroptosis of UVB-irradiated HEK is accompanied by an increase in ROS and lipid peroxidation, and a decrease of the available GSH. Either a drop in GSH supply or an increase in its utilization may cause glutathione system imbalance. Consistent with previous reports, we did not detect changes in SLC7A11 or system x_C^- levels after UVB irradiation [42]. However, it is possible that system x_C^- activity may be altered in the irradiated cells, perhaps due to excessive accumulation of oxidized phospholipid species in cell membrane, reducing the influx of cystine precursor of GSH. A decrease in cystine uptake by the keratinocytes after UVB was previously reported [42], and we found that an excess extracellular cystine had a modest effect on HEK rescue from ferroptosis. This suggests that cystine transport may be one rate limiting step in the maintenance of GSH after UVB.

An increase in GSH consumption precipitated by excessive lipid peroxidation may also explain keratinocyte susceptibility to ferroptosis,

as both radical scavengers (Fer-1, Lip-1) and the inhibitors of 15-HpETE-PE synthesis (triacsin C, baicalein) were able to maintain GSH level and prevent cell death after UVB. Consistently with previous reports, gene expression of ACSL4, 15-LOX and GPX4 increased after UVB, but on the protein level we detected an increase of ACSL4 and a decrease of GPX4 [70,71]. Interestingly, levels of ACSL4 and GPX4 in HEK and HEE correlated with UVB-induced accumulation of lipid peroxidation products and cell viability, suggesting that the balance between pro-ferroptosis death signal generation and neutralization dictates keratinocyte susceptibility to ferroptosis.

In addition to uncovering ferroptotic death of irradiated HEK, we confirmed previous reports which linked keratinocyte apoptosis and pyroptosis to UVB exposure [2,14–16,46]. Important distinctions have to be made between the execution of ferroptosis versus other RCD pathways. First, the level of oxidation of phospholipids in ferroptosis far exceeds that of apoptosis, necroptosis and pyroptosis, and PEox species are specific to ferroptosis [39]. Second, while an increase in ROS is common to all RCD, excessive PL oxidation has only been detected in ferroptosis and non-canonical pyroptosis [39]. Third, Fer-1 does not rescue cells from apoptosis, necroptosis or pyroptosis; it decreases both ROS and PLox and protects cells from ferroptosis, where these species are functionally linked and directly implicated in cell death execution.

By directly comparing Fer-1 with ZVF we confirmed their orthogonal effects on lipid peroxidation- and caspase-mediated RCD, respectively. While ZVF inhibits the activation of all caspases, apoptosis-triggering non-inflammatory and pyroptosis-triggering inflammatory types, it does not significantly reduce PLox as does Fer-1. We found that inhibition of HEK apoptosis by ZVF after UVB did not alter skin inflammation, consistent with general consensus of apoptosis being a non-immunogenic RCD. Pyroptosis, however, is a caspase-dependent immunogenic RCD. Nevertheless, inability of ZVF to inhibit HMGB1 release from irradiated HEK or to prevent UVB-induced cutaneous inflammation suggests that ferroptosis, not pyroptosis, is the primary cell death pathway responsible for skin necroinflammation after UVB exposure.

The effect of Fer-1 on caspase activation is more complex. Fer-1 has been shown to localize to mitochondria, but its activity there did not contribute to ferroptosis protection [72]. On the other hand, mitochondria-targeted nitroxides are potent ferroptosis inhibitors, suggesting that mitochondrial lipid peroxidation is necessary for ferroptosis execution [73]. We found that Fer-1 inhibits UVB-induced oxidation of CLs in HEE, but CLox species were not detected in the irradiated HEK. While CLox species are required for cytochrome *c* leakage and the execution of apoptosis [40], our observation that Fer-1 was unable to prevent caspase-3 activation after UVB argues that in HEK, as in other cell types [39], Fer-1 does not inhibit either apoptosis or pyroptosis. However, Fer-1 inhibited UVB-triggered inflammasome-dependent caspase-1 activation and cleavage of pro-IL-1β, as well as the release of HMGB1. Our data is consistent with the emerging link between lipid peroxidation and inflammasome activation demonstrated in sepsis [45,74]. Further work is required to elucidate the connection between lipid peroxidation, inflammasome activation and ferroptosis-induced inflammation.

The short-term response to DAMPs released by UVR-damaged keratinocytes is mediated by the innate immune system and involves the recruitment of neutrophils, macrophages and other myeloid cells [50]. We have determined that an acute inflammatory response to UVB in the skin, which includes the upregulation of IL6, IL-1β, IL10, IL18, IFN-β and the recruitment of myeloid cells, is significantly dampened by topical application of Fer-1 but not ZVF. Taken together, our in vitro and in vivo results suggest that acute UVB-induced necroinflammation in the skin is predominantly driven by excessive lipid peroxidation and ferroptotic death of the keratinocytes. To date, ferroptosis has been implicated in a number of diseases, and ferroptosis inhibitors such as Fer-1 have shown significant pre-clinical benefit in the treatment of acute kidney injury, intracerebral hemorrhage-induced brain injury, spinal cord injury and

radiation-induced lung fibrosis [75–78]. In all these examples, ferroptosis inhibitors were able to alleviate tissue injury and accelerate recovery by exerting an anti-inflammatory effect [32]. In line with these findings, our results implicate ferroptosis in UVB-induced skin injury and inflammation, and provide an explanation how immune modulation by regulated necrosis of the keratinocytes may promote skin cancer and exacerbate lupus and other skin diseases. Additional studies are required to better understand the relevance of keratinocyte ferroptosis in UVR-mediated skin pathology. As ferroptosis is amenable to inhibition, therapeutic modalities targeting ferroptosis in the skin should be explored for a broad range of conditions where UVB causes disease-promoting cutaneous inflammation.

4. Materials and methods

4.1. Human skin explants

Tissue samples of the normal human skin were collected after obtaining signed informed consent. The study of the collected tissue was approved by the Institutional Review Board of the University of Pittsburgh (PRO15100580). To obtain epidermal sheets (human epidermal explants - HEE), full thickness skin explants were cut and incubated in 1 U/mL dispase in DMEM/F-12 (StemCell Technologies) for 7 h at 37C. Intact epidermal sheets were separated from the dermis, and treated with either vehicle (DMSO), Fer-1 (10 μM) or z-VAD-fmk (20 μM) for 12–16 h. HEE were exposed to UVB (5 kJ/m^2), and utilized for redox lipidomics or further incubated for 4 h with inhibitors to assess HMGB1 release. Supernatants were concentrated at 3000g using 3 kDa Amicon Ultra filter (Millipore) prior to Western blotting. Irradiance of 17.4 W/m^2 (UVB - 310 nM) and 5.78 W/m^2 (UVA - 365 nm) was used (UV-2 irradiation system, Tyler Research Corporation).

4.2. Animals

All studies were conducted in accordance with the NIH guidelines for the Care and Use of Laboratory Animals and approved by the Institutional Animal Care and Use Committee of the University of Pittsburgh (Pittsburgh, PA). C57Bl/6 mice were purchased from the Jackson Laboratory. Topical treatment was performed on dorsal shaved skin, 200 μl total volume, twice within 24 h prior to UVB exposure. Vehicle control (DMSO in 70% ethanol), 10 μM ferrostatin-1 (Sigma) in 70% ethanol, and 20 μM z-VAD-fmk (Apexbio) in 70% ethanol were used. Mice were exposed to UVB (5 kJ/m^2) and after 16 h the irradiated skin was collected.

4.3. Primary human cells

Primary human epidermal keratinocytes - HEK (ATCC) and melanocytes (ATCC) were cultured using Dermal Cell Basal Medium (ATCC, PCS-200-030) with melanocyte (LifeLine Cell Technology) or keratinocyte (ATCC, PCS-200-040) growth factor kits, respectively, and Antibiotic Antimycotic solution (Sigma) and kept at passage 10 or below for all experiments. Cells were passaged weekly for cell culture maintenance using Trypsin-EDTA for Primary Cells (ATCC) and Trypsin Neutralizing Solution (ATCC) and supplemented with fresh media biweekly. For all assays, cells were used at 70% confluency.

4.4. Cell viability

HEK and melanocytes were plated in 96-wells (1 × 10 [4] cells/well) 12–16 h at 37C with ferrostatin-1 (Sigma, 10 μM), liproxstatin-1 (Tocris, 1 μM), baicalein (Tocris, 5 μM), triacsin C (Cayman Chem, 10 μM), z-VAD-fmk (Apexbio, 20 μM), deferoxamine mesylate (Sigma, 5 and 10 μM). Plates were exposed to UVA (20 kJ/m^2) or UVB (2–10 kJ/m^2), incubated 6 h at 37C, and viability was assessed with CellTiter 96 Aqueous Cell Proliferation Assay kit (MTS, Promega) according to

manufacturer protocol, by 490 nm absorbance measured with SpectraMax iD5 (Molecular Devices) microplate reader. Alternatively, Fixable Viability Dye eFluor 780 (Invitrogen) was used to assess viability by flow cytometry at 6 h, 24 h and 48 h after irradiation.

4.5. Flow cytometry

HEK were cultured in 6-well plates for at least 24 h, incubated 16 h with Fer-1 or z-VAD-fmk, and exposed to UVB (10 kJ/m^2). After 6 h, cells were washed, detached with trypsin, and incubated in PBS with FAM-YVAD-FMK (Active Caspase-1 Staining Kit, Abcam, ab219935, 1:150), C11-BODIPY 581/591 (Invitrogen, D3861, 10 μM) or Red-DEVD-FMK (CaspGLOW Red Active Caspase-3 Staining Kit, BioVision, K193, 1:100) at 37C for 1 h, followed by staining with Fixable Viability Dye eFluor 780 (Invitrogen, 1:1000) at 4C for 30 min. For intracellular proteins, cells were first stained with FVD, then treated with Reagent A Fix&Perm Kit (ThermoFisher) for 15 min RT and stained for GPX4, ACLS4 and 4-HNE for 60 min at 4C in Reagent B (Fix&Perm Kit). Anti-rabbit IgG-PerCP (Jackson ImmunoResearch, 1:100) was used as a secondary antibody for 4-HNE. To characterize the immune cell infiltrate of mouse skin, UVB-exposed skin of C57Bl/6 mice was harvested, incubated in DMEM containing collagenase D (1 mg/mL) and DNase (1 mg/mL) for 45 min at 37C. Digested tissue was passed through 70 μm cell strainer, and stained with antibodies (Supplementary Table S1) for 1 h at 4C. Flow cytometry was performed on BD LSRFortessa (BD Biosciences), and data analyzed using FlowJo software.

4.6. Western blotting

Total protein was isolated using RIPA buffer (ThermoFisher) containing protease inhibitors and phosphatase inhibitors (ThermoFisher). Cells were lysed for 30 min on ice, sonicated, and lysates were centrifugation. Protein concentrations were determined using BCA kit (ThermoFisher). Samples were heated in loading buffer at 80 °C for 5 min, and 80 μg of total protein were separated on 15% SDS polyacrylamide gel and transferred to a PVDF membrane. Membranes were blocked with Odyssey Blocking Buffer (LI-COR Biosciences) for 1 h, RT, and probed with primary antibodies (Supplementary Table S2) 16 h at 4C. Membranes were washed three times with PBST buffer for 10 min, followed by incubation with fluorescently labeled secondary antibodies (LI-COR) for 1 h at RT. Membranes were scanned on Odyssey Scanner (LI-COR). Densitometry measurements on the immunoreactive bands were performed using ImageJ software, with β-actin and GAPDH as controls.

4.7. ROS measurements

Intracellular ROS was measured using 2',7'-dichlorodihydrofluorescein diacetate (H$_2$DCFDA, Invitrogen). Cells were incubated for 16 h at 15,000 cells/well in 96-well plates with black polystyrene bottoms (Corning), with an appropriate inhibitor. Cells were then washed, stained with 50 μM H$_2$DCFDA probe for 1 h at 37C, exposed to UVB, and fluorescence measured.

4.8. Fluorescence microscopy

HEK were plated in Nunc Lab-Tek II Chamber Slides (ThermoFisher) at 5 × 10 [4] cells/well for 48 h, treated for 24 h with Fer-1 or z-VAD-fmk, exposed to UVB and incubated for 6 h at 37C. Cells were stained with C11-BODIPY 581/591 sensor (ThermoFisher) according to vendor's protocol, fixed with 2% paraformaldehyde (PFA), permeabilized with 0.1% Triton X-100 in PBS for 20 min, blocked with goat serum/2% BSA in PBS for 45 min and washed with 0.5% BSA in PBS. Cell were stained for Anti-HNE-Michael Adducts (Millipore, 1:100), Phalloidin DyLight 633 (ThermoFisher, 1:100), and with 1 μg/ml 4′,6-diamidino-2-phenylindole (DAPI). UVB-irradiated full thickness human skin explants or mouse skin was fixed with 2% PFA for 2 h and treated

with 30% sucrose in PBS for 24 h. Fresh tissue was treated with C11-BODIPY 581/591 sensor (ThermoFisher) prior to fixation. Specimens were frozen in 2-methylbutane (Sigma) in liquid nitrogen, embedded in Tissue Plus OCT (Thermo Fisher), and processed into 10 μm thick sections. Immunostaining was performed for Anti-HNE-Michael Adducts, GPX4 and ACSL4 16 h at 4C, followed by AlexaFluor 488 and Cy5-labeled secondary antibodies, Phalloidin DyLight 633, and DAPI. Sections mounted in gelvatol medium (Sigma) were imaged using Nikon A1+ confocal microscope at the Center for Biological Imaging (University of Pittsburgh, PA). Image processing and intensity analysis were performed with NIS-Elements AR 4.40 software (Nikon).

4.9. RNA isolation and quantitative RT-PCR

Total RNA was isolated from cells using TRIzol Reagent (Thermo Fisher) as per the manufacturer's instructions and quantified using a DeNovix DS-11 spectrophotometer. For cDNA synthesis, 2 μg RNA was converted to cDNA using a Quanti Tect Reverse Transcription Kit (Qiagen). For total RNA extraction from skin, tissue stored in RNAlater (Ambion) were homogenized in TRIzol Reagent using a bead homogenizer in addition to the protocol followed for cultured cells. Quantitative RT-PCR was performed using TaqMan Fast Advanced Master mix (Applied Biosystems) and TaqMan gene expression assays for IL-10, IL-6, IL-18, and IL-1β (Integrated DNA Technologies) and beta-actin (Applied Biosystems). Primer/probes for target genes (Supplementary Table S3) were FAM-ZEN/IBFQ labeled, and for actin (control) were VIC-MGB-PL labeled. Duplex reactions (target gene + actin) were run and analyzed on a StepOnePlus (Applied Biosystems). Relative fold changes were calculated and normalized based on $2^{-\Delta\Delta Ct}$ method.

4.10. Glutathione measurement

HEK were sonicated in ice-cold PBS for 2 min and centrifuged at 3000g for 5 min at 4C. Epidermal sheets were resuspended in NAVYR1-RNA lysis tubes (NextAdvance) in ice-cold PBS with proteinase inhibitor, and homogenized using Bullet Blender (NextAdvance) for 5 min. Samples were sonicated on ice for 2 min, centrifugated twice for 10 min at 8000g, and supernatants collected. Low molecular weight thiols (total thiols) were assessed with Thiol Probe IV (Millipore, 10 μM) at RT for 30 min. Total thiols were measured in untreated supernatant, and separately after incubating the supernatant with 1U glutathione peroxidase from bovine erythrocytes (Sigma) and cumene hydroperoxide (Sigma, 2.5 mM) to convert GSH to GSSG. GSH was determined as the difference between these two measurements, and normalized to total protein determined with QuantiPro BCA Assay Kit (ThermoFisher). Erastin (10 μM, Sigma) was used as control for GSH depletion. Data was collected using SpectraMax iD5 microplate reader (Molecular Devices) at 488 nm/525 nm with 515 nm cutoff.

4.11. Redox lipidomics LC-MS analysis

HEK and HEE were processed as described above and flash frozen in liquid nitrogen. Lipids were extracted using the Folch procedure, and phosphorus was determined by a micro-method as described previously [79]. Phospholipids were analyzed by LC/MS using a Dionex Ultimate 3000 HPLC system coupled on-line to a Orbitrap Fusion Lumos mass spectrometer (ThermoFisher) using a normal phase column (Luna 3 μm Silica (2) 100 Å, 150 × 2.0 mm, (Phenomenex)). The analysis was performed using gradient solvents (A and B) containing 10 mM ammonium formate at a flow rate of 0.2 ml/min. Solvent A contained isopropanol/hexane/water (285:215:5, v/v/v), and solvent B contained isopropanol/hexane/water (285:215:40, v/v/v). All solvents were LC/MS-grade. The column was eluted for 0–23 min with a linear gradient from 10% to 32% B; 23–32 min with a linear gradient of 32%–65% B; 32–35 min with a linear gradient of 65%–100% B; 35–62 min

held at 100% B; 62–64 min with a linear gradient from 100% to 10% B; followed by an equilibration from 64 to 80 min at 10% B. Analysis was performed in negative ion mode at a resolution of 140,000 for the full MS scan in a data-dependent mode. Analysis of raw LC/MS data was performed using software package Compound Discoverer™ 2.0 (ThermoFisher) with an in-house generated analysis workflow and oxidized PL database. Briefly, peaks with S/N ratio of more than 3 were identified and searched against oxidized PL database. Lipids were further filtered by retention time and confirmed by a fragmentation mass spectrum. Values for m/z were matched within 5 ppm to identify the lipid species. Peak areas were used for quantification of oxygenated PL species. Data were presented as pmol normalized to μmol of total PLs. Deuterated phospholipids 1-hexadecanoyl(d31)-2-(9Z-octadecenoyl)-sn-glycero-3-phosphoethanolamine (PE(16:0D31/18:1)), 1-hexadecanoyl(d31)-2-(9Z-octadecenoyl)-sn-glycero-3-phosphocholine (PC(16:0D31/18:1)), 1-hexadecanoyl(d31)-2-(9Z-octadecenoyl)-sn-glycero-3-phosphoserine (PS(16:0D31/18:1)), 1-hexadecanoyl(d31)-2-(9Z-octadecenoyl)-sn-glycero-3-phosphate (PA(16:0D31/18:1)), 1-hexadecanoyl(d31)-2-(9Z-octadecenoyl)-sn-glycero-3-phosphoglycerol (PG(16:0D31/18:1)), 1-hexadecanoyl(d31)-2-(9Z-octadecenoyl)-sn-glycero-3-phospho(1'-myo-inositol) (PI(16:0D31/18:1)) and 1,1',2,2'-tetramyristoyl-cardiolipin (sodium salt) (Avanti Polar Lipids) were used as internal standards. Internal standards were added directly to the MS sample to a final concentration of 1 μM. To quantitate oxygenated PL species, calibration curves were obtained using 1-stearoyl-2-15(S)-HpETE-sn-glycero-3-phosphoethanolamine and 1-stearoyl-2-15(S)-HETE-sn-glycero-3-phospho-ethanolamine, stearoyl-2-15(S)-HpETE-sn-glycero-3-phospho choline and 1-stearoyl-2-15(S)-HETE-sn-glycero-3-phosphocholine (Cayman Chemicals) and in-house biosynthesized 1-linoleoyl-1'-13-HpODE-2-linoleoyl-2'-linoleoyl-cardiolipin, 1-linoleoyl-1'-13-HO-DE-2-linoleoyl-2'-linoleoyl-cardiolipin, 1-linoleoyl-1'-13-HpODE-2-linoleoyl-2'-13-HpODE-cardiolipin, 1-linoleoyl-1'-13-HODE-2-linoleoyl-2'-13-HODE-cardiolipin. Briefly, tetra-linoleoyl-CL (TLCL) was oxidized by 15-LOX from Glycine max (soybean) (Cayman Chemicals) in 25 mM borate buffer, pH 9, in the presence of 200 μM DTPA, 0.05% sodium cholate, 5 μM H_2O_2 at RT for 45 min. The incubation mixture was continuously bubbled with 95% O_2. At the end of incubation, TLCL-OOH/TLCL-OH were extracted and purified by HPLC using 4.4 × 150 mm 5 μm C18 column (Phenomenex). SIMCA 16.1 software (Sartorius) was used to further characterize lipid profiles in HEK.

4.12. Targeted SIM and MS/MS analysis of oxygenated PLs

PLs were separated by solid phase extraction (SPE) using a sequential combination of silica gel/aminopropyl-silica gel SPE cartridges as described [80]. PE fraction was concentrated by a gentle stream of nitrogen to complete dryness and then was taken up in 20 μL of 100% of mobile phase B (see below). PE fraction was mixed carefully on a vortex to completely dissolve the analytes and then analyzed by LC/MS/MS. The injection volume was 5 μL. PE species were separated on a C30 reverse phase column (Accucore, 2.1 mm × 25 cm, 2.6 μm particle size, Thermo Scientific). Solvent A: acetonitrile/water (50/50); Solvent B: 2-propanol/acetonitrile/water (85/10/5). Both A and B solvents contained 5 mM ammonium formate and 0.1% formic acid as modifiers. Gradient method was as follows: 0–40 min, 15%–50% B (linear, 5); 40–130 min, 50–100% B (linear, 5); 130–135 min, hold at 100% B; 135–140 min, 15% B (linear, 5); 140–150 min, 15% B for equilibration. The flow was maintained at 100 ul/min. The LC system was a Thermo Ultimate 3000 complete with a WPS-3000 autosampler. Column temperature was set at 35C. Targeted (tSIM) and MS/MS analysis of specific oxidized masses was performed on a Fusion Lumos tribrid mass spectrometer (Thermo). A tSIM analysis (isolation mode quadrupole) for ions of m/z 796.5134 and 798.5193 in negative ion mode (profile) was performed at a resolution of 120,000. The maximum injection time of 128 ms with 1 microscan and a normalized AGC target of 400% using the orbitrap as the detector. MS [2] analysis was performed using high

energy collisional dissociation (HCD) with collision energy set to 24 with an isolation window of 1.2 m/z and a resolution of 30,000, also using the orbitrap as the detector. Capillary spray voltage was set at 3900V, and ion transfer tube temperature was 300C. Sheath, auxiliary and sweep gasses were set to 30, 23 and 1 (arbitrary units), respectively.

Statistical analysis

Results are expressed as mean ± SEM. Three or more groups with one independent variable were analyzed using one-way ANOVA with Tukey's multiple comparisons test. Analyses were performed using GraphPad Prism software. All tests were two-tailed and a P value < 0.05 was considered to indicate statistical significance.

Funding sources

Author contributions

Performed experiments – KV, OK, AM, SNS, AAA, VAT, YYT, YLB. Analyzed data – KV, OK, AM, SNS, AAA, VAT, YYT, VEK, YLB. Wrote or edited the manuscript – KV, OK, AM, YYT, VEK, YLB.

Declaration of competing interest

The authors declare no conflict of interest.

Appendix A. Supplementary data

Supplementary data to this article can be found online at https://doi.org/10.1016/j.redox.2021.102143.

References

[1] T.L. de Jager, A.E. Cockrell, S.S. Du Plessis, Ultraviolet light induced generation of reactive oxygen species, Adv. Exp. Med. Biol. 996 (2017) 15–23.
[2] D. Kulms, E. Zeise, B. Poppelmann, T. Schwarz, DNA damage, death receptor activation and reactive oxygen species contribute to ultraviolet radiation-induced apoptosis in an essential and independent way, Oncogene 21 (2002) 5844–5851.
[3] M. Ichihashi, et al., UV-induced skin damage, Toxicology 189 (2003) 21–39.
[4] J. D'Orazio, S. Jarrett, A. Amaro-Ortiz, T. Scott, UV radiation and the skin, Int. J. Mol. Sci. 14 (2013) 12222–12248.
[5] A. Kuhn, J. Wenzel, H. Weyd, Photosensitivity, apoptosis, and cytokines in the pathogenesis of lupus erythematosus: a critical review, Clin. Rev. Allergy Immunol. 47 (2014) 148–162.
[6] R. Caricchio, L. McPhie, P.L. Cohen, Ultraviolet B radiation-induced cell death: critical role of ultraviolet dose in inflammation and lupus autoantigen redistribution, J. Immunol. 171 (2003) 5778–5786.
[7] T. Bald, et al., Ultraviolet-radiation-induced inflammation promotes angiotropism and metastasis in melanoma, Nature 507 (2014) 109–113.
[8] M. Neagu, et al., Inflammation: a key process in skin tumorigenesis, Oncol Lett 17 (2019) 4068–4084.
[9] K.E. Johnson, B.C. Wulff, T.M. Oberyszyn, T.A. Wilgus, Ultraviolet light exposure stimulates HMGB1 release by keratinocytes, Arch. Dermatol. Res. 305 (2013) 805–815.
[10] A.T. Black, et al., UVB light upregulates prostaglandin synthases and prostaglandin receptors in mouse keratinocytes, Toxicol. Appl. Pharmacol. 232 (2008) 14–24.
[11] A. Nicolaou, S.M. Pilkington, L.E. Rhodes, Ultraviolet-radiation induced skin inflammation: dissecting the role of bioactive lipids, Chem. Phys. Lipids 164 (2011) 535–543.
[12] M. Yoshizumi, et al., Release of cytokines/chemokines and cell death in UVB-irradiated human keratinocytes, HaCaT. *Cell Biol Int* 32 (2008) 1405–1411.
[13] A.W. Borkowski, R.L. Gallo, UVB radiation illuminates the role of TLR3 in the epidermis, J. Invest. Dermatol. 134 (2014) 2315–2320.

[14] N. Pustisek, M. Situm, UV-radiation, apoptosis and skin, Coll. Antropol. 35 (Suppl 2) (2011) 339–341.
[15] A. Van Laethem, M. Garmyn, P. Agostinis, Starting and propagating apoptotic signals in UVB irradiated keratinocytes, Photochem. Photobiol. Sci. 8 (2009) 299–308.
[16] G. Sollberger, et al., Caspase-1 activity is required for UVB-induced apoptosis of human keratinocytes, J. Invest. Dermatol. 135 (2015) 1395–1404.
[17] I.K. Poon, C.D. Lucas, A.G. Rossi, K.S. Ravichandran, Apoptotic cell clearance: basic biology and therapeutic potential, Nat. Rev. Immunol. 14 (2014) 166–180.
[18] L. Galluzzi, A. Buque, O. Kepp, L. Zitvogel, G. Kroemer, Immunogenic cell death in cancer and infectious disease, Nat. Rev. Immunol. 17 (2017) 97–111.
[19] R.E. Voll, et al., Immunosuppressive effects of apoptotic cells, Nature 390 (1997) 350–351.
[20] C.G. Freire-de-Lima, et al., Apoptotic cells, through transforming growth factor-beta, coordinately induce anti-inflammatory and suppress pro-inflammatory eicosanoid and NO synthesis in murine macrophages, J. Biol. Chem. 281 (2006) 38376–38384.
[21] Z. Szondy, Z. Sarang, B. Kiss, E. Garabuczi, K. Koroskenyi, Anti-inflammatory mechanisms triggered by apoptotic cells during their clearance, Front. Immunol. 8 (2017) 909.
[22] M. Sarhan, W.G. Land, W. Tonnus, C.P. Hugo, A. Linkermann, Origin and consequences of necroinflammation, Physiol. Rev. 98 (2018) 727–780.
[23] Y. Yang, G. Jiang, P. Zhang, J. Fan, Programmed cell death and its role in inflammation, Mil Med Res 2 (2015) 12.
[24] J. Shi, et al., Cleavage of GSDMD by inflammatory caspases determines pyroptotic cell death, Nature 526 (2015) 660–665.
[25] J. Seo, Y.W. Nam, S. Kim, D.B. Oh, J. Song, Necroptosis molecular mechanisms: Recent findings regarding novel necroptosis regulators, Exp. Mol. Med. 53 (2021) 1007–1017.
[26] M. Conrad, D.A. Pratt, The chemical basis of ferroptosis, Nat. Chem. Biol. 15 (2019) 1137–1147.
[27] B.R. Stockwell, et al., Ferroptosis: a regulated cell death nexus linking metabolism, redox biology, and disease, Cell 171 (2017) 273–285.
[28] J.P. Friedmann Angeli, et al., Inactivation of the ferroptosis regulator Gpx4 triggers acute renal failure in mice, Nat. Cell Biol. 16 (2014) 1180–1191.
[29] M.M. Gaschler, et al., FINO2 initiates ferroptosis through GPX4 inactivation and iron oxidation, Nat. Chem. Biol. 14 (2018) 507–515.
[30] W.S. Yang, et al., Regulation of ferroptotic cancer cell death by GPX4, Cell 156 (2014) 317–331.
[31] V.E. Kagan, Oxidized arachidonic and adrenic PEs navigate cells to ferroptosis, Nat. Chem. Biol. 13 (2017) 81–90.
[32] Y. Sun, et al., The emerging role of ferroptosis in inflammation, Biomed. Pharmacother. 127 (2020) 110108.
[33] M. Yoshida, et al., Involvement of cigarette smoke-induced epithelial cell ferroptosis in COPD pathogenesis, Nat. Commun. 10 (2019) 3145.
[34] M. Xu, et al., Ferroptosis involves in intestinal epithelial cell death in ulcerative colitis, Cell Death Dis. 11 (2020) 86.
[35] M. Telorack, et al., A glutathione-Nrf2-Thioredoxin Cross-Talk ensures keratinocyte survival and efficient wound repair, PLoS Genet. 12 (2016), e1005800.
[36] C. Wenz, et al., Cell-cell contacts protect against t-BuOOH-induced cellular damage and ferroptosis in vitro, Arch. Toxicol. 93 (2019) 1265–1279.
[37] G.P. Drummen, L.C. van Liebergen, J.A. Op den Kamp, J.A. Post, C11-BODIPY (581/591), an oxidation-sensitive fluorescent lipid peroxidation probe: (micro) spectroscopic characterization and validation of methodology, Free Radic. Biol. Med. 33 (2002) 473–490.
[38] C. Schneider, N.A. Porter, A.R. Brash, Routes to 4-hydroxynonenal: fundamental issues in the mechanisms of lipid peroxidation, J. Biol. Chem. 283 (2008) 15539–15543.
[39] B. Wiernicki, et al., Excessive phospholipid peroxidation distinguishes ferroptosis from other cell death modes including pyroptosis, Cell Death Dis. 11 (2020) 922.
[40] V.E. Kagan, et al., Cytochrome c acts as a cardiolipin oxygenase required for release of proapoptotic factors, Nat. Chem. Biol. 1 (2005) 223–232.
[41] G. Mao, et al., Mitochondrial redox opto-lipidomics reveals mono-oxygenated cardiolipins as pro-apoptotic death signals, ACS Chem. Biol. 11 (2016) 530–540.
[42] M. Zhu, G.T. Bowden, Molecular mechanism(s) for UV-B irradiation-induced glutathione depletion in cultured human keratinocytes, Photochem. Photobiol. 80 (2004) 191–196.
[43] P.H. Chen, W.H. Tseng, J.T. Chi, The intersection of DNA damage response and ferroptosis-A rationale for combination therapeutics, Biology 9 (2020).
[44] O. Canli, et al., Glutathione peroxidase 4 prevents necroptosis in mouse erythroid precursors, Blood 127 (2016) 139–148.
[45] R. Kang, et al., Lipid peroxidation drives gasdermin D-mediated pyroptosis in lethal polymicrobial sepsis, Cell Host Microbe 24 (2018) 97–108, e104.
[46] Y. Chen, et al., Ultraviolet B induces proteolytic cleavage of the pyroptosis inducer gasdermin E in keratinocytes, J. Dermatol. Sci. 100 (2) (2020) 160–163.
[47] M. Kennedy Crispin, et al., Gene profiling of narrowband UVB-induced skin injury defines cellular and molecular innate immune responses, J. Invest. Dermatol. 133 (2013) 692–701.
[48] L. Feldmeyer, et al., The inflammasome mediates UVB-induced activation and secretion of interleukin-1beta by keratinocytes, Curr. Biol. 17 (2007) 1140–1145.
[49] D. Cho, et al., The enhanced IL-18 production by UVB irradiation requires ROI and AP-1 signaling in human keratinocyte cell line (HaCaT), Biochem. Biophys. Res. Commun. 298 (2002) 289–295.
[50] J.J. Bernard, R.L. Gallo, J. Krutmann, Photoimmunology: how ultraviolet radiation affects the immune system, Nat. Rev. Immunol. 19 (2019) 688–701.
[51] P.H. Hart, M. Norval, Ultraviolet radiation-induced immunosuppression and its relevance for skin carcinogenesis, Photochem. Photobiol. Sci. 17 (2018) 1872–1884.
[52] H. McGrath Jr., Ultraviolet-A1 irradiation therapy for systemic lupus erythematosus, Lupus 26 (2017) 1239–1251.
[53] P. Wolf, W. Weger, V. Patra, A. Gruber-Wackernagel, S.N. Byrne, Desired response to phototherapy vs photoaggravation in psoriasis: what makes the difference? Exp. Dermatol. 25 (2016) 937–944.
[54] R.L. Gallo, J.J. Bernard, Innate immune sensors stimulate inflammatory and immunosuppressive responses to UVB radiation, J. Invest. Dermatol. 134 (2014) 1508–1511.
[55] X. Huang, A.N. Chalmers, Review of wearable and portable sensors for monitoring personal solar UV exposure, Ann. Biomed. Eng. 49 (2021) 964–978.
[56] D.L. Rodenbeck, J.I. Silverberg, N.B. Silverberg, Phototherapy for atopic dermatitis, Clin. Dermatol. 34 (2016) 607–613.
[57] A.S. Gary, P.J. Rochette, Apoptosis, the only cell death pathway that can be measured in human diploid dermal fibroblasts following lethal UVB irradiation, Sci. Rep. 10 (2020) 18946.
[58] L. Liu, et al., Keratinocyte-derived microvesicle particles mediate ultraviolet B radiation-induced systemic immunosuppression, J. Clin. Invest. 131 (2021).
[59] K.L. Cooper, J.W. Yager, L.G. Hudson, Melanocytes and keratinocytes have distinct and shared responses to ultraviolet radiation and arsenic, Toxicol. Lett. 224 (2014) 407–415.
[60] B.M. Aufiero, et al., Narrow-band UVB induces apoptosis in human keratinocytes, J. Photochem. Photobiol., B 82 (2006) 132–139.
[61] J.Y. Cao, S.J. Dixon, Mechanisms of ferroptosis, Cell. Mol. Life Sci. 73 (2016) 2195–2209.
[62] S.E. Wenzel, et al., PEBP1 wardens ferroptosis by enabling lipoxygenase generation of lipid death signals, Cell 171 (2017) 628–641 e626.
[63] T.S. Anthonymuthu, et al., Resolving the paradox of ferroptotic cell death: ferrostatin-1 binds to 15LOX/PEBP1 complex, suppresses generation of peroxidized ETE-PE, and protects against ferroptosis, Redox Biol 38 (2021) 101744.
[64] G. Miotto, et al., Insight into the mechanism of ferroptosis inhibition by ferrostatin-1, Redox Biol 28 (2020) 101328.
[65] M.S. Narzt, et al., A novel role for NUPR1 in the keratinocyte stress response to UV oxidized phospholipids, Redox Biol 20 (2019) 467–482.
[66] Y. Zhao, et al., Autophagy is induced by UVA and promotes removal of oxidized phospholipids and protein aggregates in epidermal keratinocytes, J. Invest. Dermatol. 133 (2013) 1629–1637.
[67] O. Sorg, et al., Effect of intense pulsed-light exposure on lipid peroxides and thymine dimers in human skin in vivo, Arch. Dermatol. 143 (2007) 363–366.
[68] Z. Ni, G. Angelidou, R. Hoffmann, M. Fedorova, LPPtiger software for lipidome-specific prediction and identification of oxidized phospholipids from LC-MS datasets, Sci. Rep. 7 (2017) 15138.
[69] Z. Ni, L. Goracci, G. Cruciani, M. Fedorova, Computational solutions in redox lipidomics - current strategies and future perspectives, Free Radic. Biol. Med. 144 (2019) 110–123.
[70] H. Yoo, B. Jeon, M.S. Jeon, H. Lee, T.Y. Kim, Reciprocal regulation of 12- and 15-lipoxygenases by UV-irradiation in human keratinocytes, FEBS Lett. 582 (2008) 3249–3253.
[71] C.D. Enk, et al., The UVB-induced gene expression profile of human epidermis in vivo is different from that of cultured keratinocytes, Oncogene 25 (2006) 2601–2614.
[72] M.M. Gaschler, et al., Determination of the subcellular localization and mechanism of action of ferrostatins in suppressing ferroptosis, ACS Chem. Biol. 13 (2018) 1013–1020.
[73] T. Krainz, et al., A mitochondrial-targeted nitroxide is a potent inhibitor of ferroptosis, ACS Cent. Sci. 2 (2016) 653–659.
[74] R. Chen, et al., AGER-mediated lipid peroxidation drives caspase-11 inflammasome activation in sepsis, Front. Immunol. 10 (2019) 1904.
[75] A. Linkermann, et al., Synchronized renal tubular cell death involves ferroptosis, Proc. Natl. Acad. Sci. U. S. A. 111 (2014) 16836–16841.
[76] Z. Zhang, et al., Glutathione peroxidase 4 participates in secondary brain injury through mediating ferroptosis in a rat model of intracerebral hemorrhage, Brain Res. 1701 (2018) 112–125.
[77] Y. Zhang, et al., Ferroptosis inhibitor SRS 16-86 attenuates ferroptosis and promotes functional recovery in contusion spinal cord injury, Brain Res. 1706 (2019) 48–57.
[78] X. Li, et al., Ferroptosis inhibitor alleviates Radiation-induced lung fibrosis (RILF) via down-regulation of TGF-beta1, J. Inflamm. 16 (2019) 11.
[79] W.Y. Sun, et al., Phospholipase iPLA2beta averts ferroptosis by eliminating a redox lipid death signal, Nat. Chem. Biol. 17 (2021) 465–476.
[80] A. Fauland, et al., An improved SPE method for fractionation and identification of phospholipids, J Sep Sci 36 (2013) 744–751.